Burlingame, CA), visualized with ECL (Amersham, Arlington Heights, IL), and quantified with ImageQuant (Molecular Dynamics).
22. M. B. Grant *et al.*, *Regul. Pept.* **48**, 267 (1993).
23. J. S. Flier and A. C. Moses, in *Endocrinology*, L. J. DeGroot, Ed. (Saunders, Philadelphia, PA, 1989), vol. 2, pp. 1389–1399.
24. C. P. Burren, J. L. Berka, S. R. Edmonson, G. A. Werther, J. A. Batch, *Invest. Ophthalmol. Visual Sci.* **37**, 1459 (1996); P. Moriarty, A. Dickson, D. McCloud, *Br. J. Ophthalmol.* **78**, 638 (1994); I. Jilial, *Endocrinology* **117**, 1222 (1985).
25. The diabetic retinopathy study research group, *Ophthalmology* **88**, 583 (1981); *Arch. Ophthalmol.* **97**, 654 (1979); Cryotherapy for retinopathy of prematurity cooperative group, *ibid.* **108**, 1408 (1990).
26. H. P. Hammes, M. Brownlee, A. Jonczyk, A. Sutter, *Nature Med.* **2**, 529 (1996).
27. Z. Laron, R. Sarel, A. Pertzelan, *Eur. J. Pediatrics* **134**, 79 (1980).
28. R. D'Amato, E. Wesolowski, L. E. Smith, *Microvasc. Res.* **46**, 135 (1993).
29. We thank X. Xu, R. Sullivan, T. Meehan, R. Webb, K. Cheng, T. W. Wu, and S. Satiritz for assistance and D. Senger and K. Claffey for helpful discussions. Supported in part by grants from the V. Kann Rasmussen Foundation and the National Eye Institute (EY08670 to L.E.H.S.) and the Ohio State Eminent Scholars Program, Sensus Corporation, and the Juvenile Diabetes International (195061 to J.J.K.).

10 February 1997; accepted 14 May 1997

Regulation of Mitochondrial Iron Accumulation by Yfh1p, a Putative Homolog of Frataxin

Michael Babcock, Deepika de Silva, Robert Oaks, Sandra Davis-Kaplan, Sarn Jiralerspong, Laura Montermini, Massimo Pandolfo, Jerry Kaplan*

The gene responsible for Friedreich's ataxia, a disease characterized by neurodegeneration and cardiomyopathy, has recently been cloned and its product designated frataxin. A gene in *Saccharomyces cerevisiae* was characterized whose predicted protein product has high sequence similarity to the human frataxin protein. The yeast gene (yeast frataxin homolog, *YFH1*) encodes a mitochondrial protein involved in iron homeostasis and respiratory function. Human frataxin also was shown to be a mitochondrial protein. Characterizing the mechanism by which *YFH1* regulates iron homeostasis in yeast may help to define the pathologic process leading to cell damage in Friedreich's ataxia.

Friedreich's ataxia (FRDA) is an autosomal recessive degenerative disease characterized by progressive gait and limb ataxia, signs of axonal sensory neuropathy, pyramidal weakness of the legs, and dysarthria (*1*). A hypertrophic cardiomyopathy is found in almost all affected individuals (*1*, *2*). Diabetes mellitus accompanied by a loss of pancreatic β cells is seen in about 10% of the cases, carbohydrate intolerance is present in an additional 20%, and all patients show abnormal insulin secretion in response to amino acid stimulation (*3*).

The molecular defect in FRDA was identified as a deficiency of frataxin, a small protein (210 amino acids) whose function could not be identified by amino acid sequence analysis (*4*). Frataxin deficiency may occasionally be traced to nonsense, splice site, or missense point mutations, but the primary cause is the hyperexpansion of a polymorphic GAA trinucleotide repeat situated in the first intron of the corresponding gene, which results in a marked reduction in the steady-state level of mature frataxin mRNA (*4*, *5*). RNA analysis of frataxin expression in adult human tissues (*4*) and in situ hybridization studies in the mouse (*6*) suggested a direct correlation between the pattern of degeneration observed in the disease and the sites of frataxin transcription, which is highest in heart, spinal cord, and dorsal root ganglia. A recent study proposed that frataxin was encoded in a larger transcriptional unit than originally thought, and that its gene was in fact part of the neighboring *STM7* gene, which was transcribed in the same direction and encoded a phosphatidylinositol 4-phosphate 5-kinase (*7*). New evidence suggests that the inclusion of *STM7* sequence as part of the FRDA gene was based on polymerase chain reaction (PCR) conditions that amplified rare and illegitimate transcripts not usually detected in vivo (*5*). All of the FRDA mutations identified to date are located in the original 3′ "frataxin" region of the gene (*4*, *5*).

Genes encoding predicted proteins with high sequence similarity to frataxin have been identified in mouse, rat, *Caenorhabditis elegans*, and an anonymous open reading frame (YDL120w) in *Saccharomyces cerevisiae* (*6*, *8*). The predicted yeast frataxin homolog was independently identified as a multicopy suppressor of a mutant (*bm-8*) that was unable to grow on iron-limited medium. The *bm-8* mutant was transformed with a genomic library, and a clone was identified that partially overcame the low-iron growth deficit (*9*). The region responsible for the complementing activity was identified by subcloning the open reading frame YDL120w on chromosome IV (*10*). BLAST analysis of this sequence identified two proteins with high sequence similarity, the predicted product of an anonymous open reading frame in the *C. elegans* genome and human frataxin. We determined that *YFH1* was not allelic to *bm-8*. First, no complementation was seen when *bm-8* was transformed with *YFH1* on a centromeric plasmid. Second, allelic segregation demonstrated that a *LEU2* marker integrated next to the chromosomal copy of *YFH1* segregated away from *bm-8* (*11*). Third, the gene allelic to *bm-8* was cloned by genomic complementation and the open reading frame (YMR134w) localized to chromosome XIII. Although these results demonstrate that *YFH1* was not responsible for the phenotype of *bm-8*, the fact that overexpression of *YFH1* alleviated the *bm-8* low-iron growth defect suggested that it was involved in iron metabolism.

To define the function of *YFH1*, we disrupted the chromosomal copy by inserting the *HIS3* auxotrophic marker into the open reading frame (*12*). Disruptants were selected and deletion of *YFH1* confirmed by Southern (DNA) analysis. The Δ*yfh1* (*yfh1*::*HIS3*) strain showed a severe growth deficit on fermentable carbon sources regardless of iron concentration. The deletion strain was unable to grow on rich medium containing glycerol and ethanol (YPGE) as the carbon source, suggesting that Δ*yfh1* was unable to carry out oxidative phosphorylation. The disruptant was also unable to grow on any media at 37°C. The respiratory incompetence of Δ*yfh1* was confirmed by demonstrating a severe reduction in oxygen consumption, even in cells grown in rich medium (*13*). We hypothesized that the Δ*yfh1* cells were unable to grow on fermentable carbon sources as a result of the generation of *rho*$^-$ mutants. These *rho*$^-$ mutations are characterized by defects in or loss of mitochondrial DNA and an inability to carry out oxidative phosphorylation. Lack of growth on respiratory substrates in Δ*yfh1* was shown to be the result of a loss of mitochondrial DNA. Diploids generated from a cross between Δ*yfh1* and wild-type cells were respiratory competent, whereas diploids from Δ*yfh1* and a *rho* tester strain (*rho*^{0}) were unable to grow on

M. Babcock, D. de Silva, R. Oaks, S. Davis-Kaplan, J. Kaplan, Division of Immunology and Cell Biology, Department of Pathology, School of Medicine, University of Utah, Salt Lake City, UT 84132, USA.
S. Jiralerspong and L. Montermini, Centre de Recherche Louis-Charles Simard, Montréal, Québec, H2L4M1 Canada.
M. Pandolfo, Department of Medicine, Université de Montréal, Montréal, Québec, H2L4M1 Canada, and Department of Neurology and Neurosurgery, McGill University, Montréal, Québec, H3A2B4 Canada.
*To whom correspondence should be addressed.

respiratory substrates. Therefore, once mitochondrial damage has occurred in Δ*yfh1*, the defect is cytoplasmically inherited and is not due to a second nuclear mutation.

These data suggest that loss of the *YFH1* gene results in a loss of mitochondrial function. To test this hypothesis, we transformed a *yfh1::HIS3/YFH1* diploid with a plasmid that contained the entire *YFH1* gene and *URA3* as a selectable marker. All of the diploids were capable of growth on YPGE. When the diploids were sporulated, tetrads segregated such that *yfh1::HIS3* cells bearing the plasmid grew well on all media, including YPGE. When the plasmid was cured by growth on 5-fluoroorotic acid, the Δ*yfh1* haploids lost the ability to use respiratory carbon sources and the slow-growth phenotype was observed on all other media. Transformation of these cells with a wild-type copy of *YFH1* restored growth on YPD medium but did not restore the ability to grow on YPGE.

Taken together, these data indicate that the Yfh1 protein (Yfh1p) is involved in iron homeostasis and mitochondrial function. PSORT analysis of the protein sequence of Yfh1p predicts a mitochondrial targeting sequence (*14*). To localize Yfh1p within the cell, we fused green fluorescent protein (GFP) to the COOH-terminus of Yfh1p expressed under the control of the methionine promoter (*15*). Plasmids bearing the Yfh1p-GFP fusion construct were transformed into Δ*yfh1* cells. The construct was able to complement fully the slow-growth phenotype of the disruptant, indicating that the fusion protein was functional in vivo. Fluorescence microscopy demonstrated that the protein was localized to the mitochondria. Co-staining of cells for porin (a mitochondrial outer membrane protein) and Yfh1p-GFP indicated that Yfh1p-GFP was not localized in the outer membrane (Fig. 1).

Because overexpression of *YFH1* alleviated the low-iron growth phenotype of *bm-8*, we examined a Δ*yfh1* strain for perturbations in iron metabolism. The entry of iron through the plasma membrane into *S. cerevisiae* grown in iron-rich medium is mediated by low-affinity transport systems. Normally, transcription of the high-affinity iron transport system, which consists of a ferroxidase (Fet3p) and permease (Ftr1p), is not detected if cells are iron replete (*9*, *16*). In Δ*yfh1* cells a marked induction of the high-affinity iron transport system was observed even when cells were grown in iron-rich medium (Fig. 2A). Northern (RNA) analysis showed a 10- to 50-fold induction of *FET3* and *FTR1* transcripts in Δ*yfh1* cells grown in YPD compared with wild-type cells, confirming the induction of the high-affinity transport system even in iron-replete conditions (Fig. 2B). As a control, mRNA was isolated from the AFT1-1^{up} strain grown in high- and low-iron media. This strain shows constitutive expression of the components of the high-affinity iron transport system due to a mutation in the transcriptional regulator *AFT1* (*17*). As shown in Fig. 2B, Δ*yfh1* had the same level of *FET3* and *FTR1* expression in YPD as did an AFT1-1^{up} strain or a maximally induced wild-type strain.

An increased rate of iron uptake, coupled with a slower rate of cell division, should be reflected by an increase in cellular iron content. Measurement of cellular iron content by atomic absorption spectroscopy revealed a doubling of iron content in Δ*yfh1* cells compared with wild-type cells (Fig. 3A). Purified mitochondria from Δ*yfh1* cells showed an iron concentration 10 times that in the mitochondria of wild-type cells. No differences were observed in the mitochondrial content of copper or calcium. Cellular and mitochondrial iron were also assayed in AFT1-1^{up} cells. This latter strain shows intracellular iron concentrations comparable with those of the Δ*yfh1* strain (Fig. 3A). The fact that AFT1-1^{up} cells had high intracellular iron but showed neither an increase in mitochondrial iron (Fig. 3B) nor a respiratory growth defect indicated that the accumulation of mitochondrial iron was specifically associated with the deletion of *YFH1* and was not simply a consequence of increased cellular iron. Accumulation of mitochondrial iron in Δ*yfh1* renders this strain hypersensitive to oxidative stress, as demonstrated by its sensitivity to H_2O_2 (Fig. 3C).

Our data indicate that *YFH1* encodes a mitochondrial protein that, when deleted, results in the accumulation of mitochondrial iron at the expense of cytosolic iron. This increase in iron compromises mitochondrial

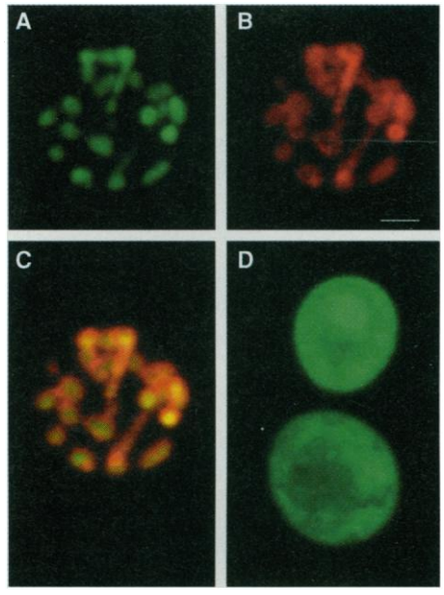

Fig. 1. Distribution of fluorescence in cells transformed with a Yfh1p–green fluorescent protein construct. (**A**) Localization of Yfh1p-GFP to the mitochondria. A wild-type strain (DY150) was transformed with the Yfh1p-GFP fusion construct, and cells were grown in YPGE medium lacking methionine, fixed, and examined by fluorescence microscopy. (**B**) Immunodetection of porin, a mitochondrial outer membrane protein. Mouse antibody to porin was used as a primary antibody (1:500 dilution), and Texas-Red goat antibody to mouse immunoglobulin G was used as a secondary antibody (1:200 dilution). (**C**) Overlay of the Yfh1p-GFP fluorescence and the porin immunostain, illustrating the different locations of the two proteins within the mitochondria. (**D**) Wild-type cells transformed with GFP alone as a control (*14*). Cells were grown on synthetic medium lacking methionine and containing glycerol and ethanol as the carbon source. The fixed cells were attached to poly-L-lysine–treated cover slips and examined by confocal laser fluorescence microscopy on a Bio-Rad MRC 600 microscope with a Nikon Optishot camera. The scale bar in (B) represents 1 μm.

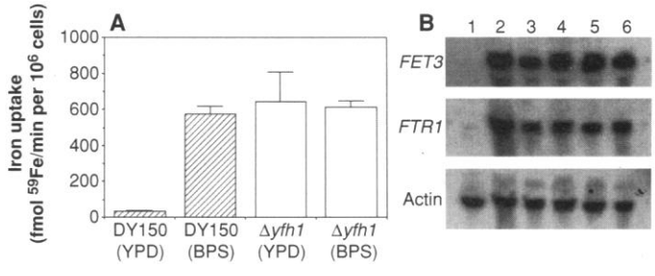

Fig. 2. Constitutive induction of the high-affinity iron transport system in Δ*yfh1* cells. (**A**) High-affinity iron uptake into whole cells. Wild-type (DY150) and Δ*yfh1* cells were grown in YPD or in iron-limited media [BPS(0)] for 6 hours. The cells were washed and assayed for ^{59}Fe transport by incubation for 10 min at 30°C in assay medium that contained 0.5 μM ^{59}Fe in the presence of 1.0 mM ascorbate as described (*9*). The data (mean ± SEM) are representative of three independent experiments. (**B**) Northern blot analysis of RNA extracted from DY150 (lanes 1 and 4), Δ*yfh1* (lanes 2 and 5), and AFT1-1^{up} cells (lanes 3 and 6) showing a constitutive induction of the components of the high-affinity iron transport system. Cells were grown in YPD (lanes 1 to 3) and BPS(0) (lanes 4 to 6), respectively, as described in (A). Northern analysis was performed and the blots probed with *FET3*, *FTR1*, and actin as described (*29*).

function and results in hypersensitivity to oxidative stress, presumably as a result of iron-catalyzed Fenton chemistry. The sensitivity of Δ*yfh1* cells to oxidative stress may explain why *rho*⁻ mutations are generated at such high frequency in this strain. Inhibition of oxidative phosphorylation may reduce the production of reactive oxygen species, such as superoxide, and attenuate the effects of mitochondrial iron accumulation.

Several lines of evidence are consistent with a mitochondrial defect underlying the etiology of FRDA. Mitochondrial dysfunction is found in several degenerative ataxias (*18*), and damage to mitochondria is also a strong apoptotic signal in neuronal cells (*19*). Variable abnormalities of several mitochondrial enzyme activities have been reported in FRDA patients (*20*), as well as perturbations in heme biosynthesis (*21*) and hypersensitivity of cultured cells to ionizing radiation (*22*). Human frataxin was also localized to the mitochondria, as shown by fluorescence microscopy analysis of cultured cells transfected with human frataxin–GFP expression constructs (Fig. 4). Mitochondrial dysfunction from iron deposition may account for the biochemical and neurological lesions seen in FRDA. Iron deposits have been found in the myocardium of FRDA patients, even in cells not yet showing signs of degeneration (*23*). Tissues most affected in FRDA are neurons and cardiac cells, which are postmitotic tissues that largely depend on efficient oxidative energy metabolism (*24*, *25*). However, this cannot fully explain the specificity of pathological involvement in FRDA, because many neuronal types, spinal cord and brainstem motor neurons for instance, are notably spared. Affected tissues appear to be those normally expressing the highest frataxin levels (*4*, *6*). In addition, vitamin E deficiency in humans, either genetic or acquired, leads to a clinicopathological picture very similar to FRDA and sometimes indistinguishable (*26*). It is possible that frataxin, by stimulating iron transport out of the mitochondria, and the antioxidant vitamin E, which localizes in mitochondrial membranes (*27*), cooperate to protect certain cell types from mitochondrial oxidative damage. There may be multiple protective antioxidant systems in humans, so other cell types may rely on different mechanisms and be unaffected by frataxin or vitamin E deficiency. Redundancy of these systems and the presence of residual frataxin in patients may in part explain the less dramatic human phenotype compared with the yeast knockout model. So far, no FRDA patients carrying null mutations in both alleles of the frataxin gene, and therefore completely lacking frataxin, have been identified. Genotype-phenotype correlation studies, however, have shown that larger GAA expansions are associated with lower residual frataxin mRNA levels and an increase in the onset and severity of the disease (*28*).

Characterization of Yfh1p, the yeast frataxin homolog, has led to the identification of an in vivo function that may explain the pathophysiology observed in FRDA. Identification of other proteins that interact with Yfh1p will provide a clearer understanding of mitochondrial iron homeostasis and the etiology of FRDA.

Note added in proof: Expression of frataxin-GFP in the Δ*yfh1* strain resulted in localization of the human protein to yeast mitochondria but was unable to complement the mutant phenotype. This result suggests that frataxin interacts specifically with mitochondrial proteins to effect iron transport and that despite strong similarity of function, proteins of the yeast and human systems are not interchangeable.

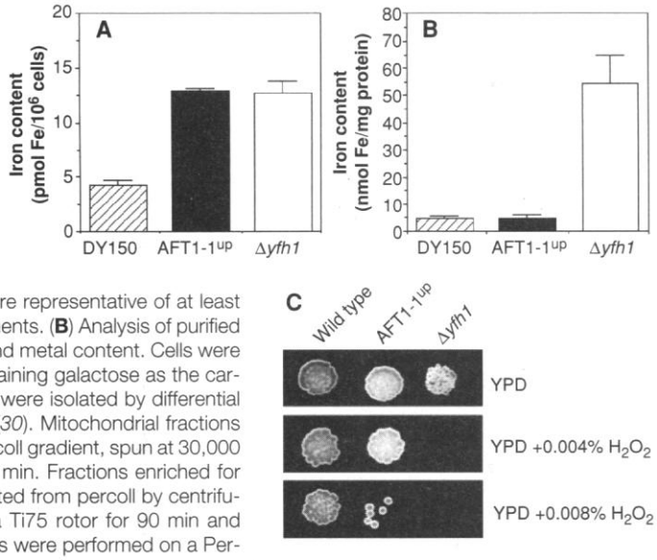

Fig. 3. Deletion of *YFH1* causes an increase in cellular and mitochondrial iron accumulation. (**A**) Analysis of cellular iron content in wild-type (DY150), Δ*yfh1*, and AFT1-1^{up} cells. Cells were grown in galactose medium and washed, and samples were analyzed for metal content. The data (mean ± SEM) are representative of at least three independent experiments. (**B**) Analysis of purified mitochondria for protein and metal content. Cells were grown in YP medium containing galactose as the carbon source. Mitochondria were isolated by differential centrifugation techniques (*30*). Mitochondrial fractions were applied to a 15% percoll gradient, spun at 30,000 rpm in a Ti75 rotor for 27 min. Fractions enriched for mitochondria were separated from percoll by centrifugation at 55,000 rpm in a Ti75 rotor for 90 min and atomic absorption analyses were performed on a Perkin-Elmer model 305A instrument. Protein determinations were performed with the BCA procedure (Pierce, Rockford, Illinois) using bovine serum albumin (fraction V) as the standard. Data are normalized to the protein content of the samples. (**C**) Sensitivity of Δ*yfh1* cells to growth on H_2O_2. Cells (10^3/10 μl) were spotted on YPD or YPD containing 0.004% or 0.008% H_2O_2 and allowed to grow for 3 days at 30°C.

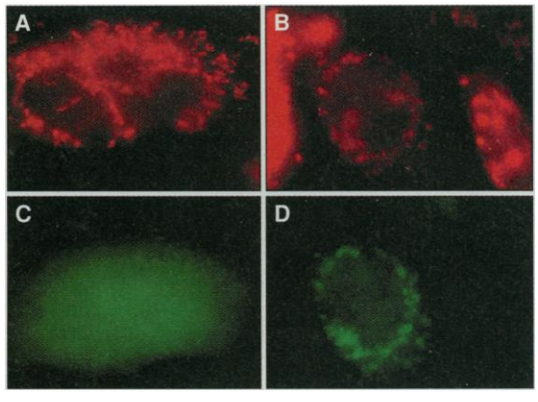

Fig. 4. Mitochondrial localization of human frataxin in live mammalian cells. Expression vectors were constructed containing sequences encoding the entire proposed human frataxin protein fused to a modified GFP tag (Clontech). Cos7 cells transfected separately with these constructs were incubated 15 min with 50 nM mitochondrial-specific MitoTracker Orange stain (Molecular Probes) 24 hours after transfection and then immediately photographed with a Zeiss MC100/Axioskop fluorescent microscope camera system with the appropriate filter sets. (**A** and **C**) Construct with GFP at the NH_2-terminus. (**B** and **D**) Construct with frataxin at the NH_2-terminus. The frataxin-GFP fusion protein with frataxin at the NH_2-terminus was targeted to organellar structures matching the appearance and distribution of mitochondria as revealed by MitoTracker staining. The frataxin-GFP fusion protein with GFP at the NH_2-terminus generated a diffuse cytosolic fluorescence, consistent with the masking by GFP of a frataxin NH_2-terminal mitochondrial targeting sequence.

REFERENCES AND NOTES

1. G. Geoffroy *et al.*, *Can. J. Neurol. Sci.* **3**, 279 (1976); A. E. Harding, *Brain* **104**, 589 (1981).
2. A. E. Harding and R. L. Hewer, *Q. J. Med.* **208**, 489 (1983).
3. G. Finocchiaro *et al.*, *Neurology* **38**, 1292 (1988).
4. V. Campuzano *et al.*, *Science* **271**, 1423 (1996).
5. M. Cossée *et al.*, *Nature Genet.* **15**, 337 (1997).
6. S. Jiralerspong *et al.*, *Neurobiol. Dis.*, in press.

7. J. Carvajal *et al.*, *Nature Genet.* **14**, 157 (1996).
8. Mouse and rat homologs were also found among sequences in the expressed sequence tag (EST) database.
9. Cells (DY150), mutagenized with ethylmethane sulfonate were subjected to a streptonigrin enrichment screen followed by replica plating on low-iron [BPS(5)] and high-iron [yeast extract, peptone, and dextrose (YPD)] plates as described by C. C. Askwith *et al.* [*Cell* **76**, 403 (1994)]. Low-iron medium was generated by using the iron chelator bathophenanthrolinedisulfonate (BPS). Numbers in parenthesis indicate exogenous iron added back in micromolar; for example, BPS (5) contains 5 μM iron. The *bm-8* mutant grew well on YPD but exhibited a marked growth defect on iron-restricted plates.
10. The mutant *bm-8* was transformed with a multicopy yeast genomic library, and the plasmid pTF63/p24 was recovered by its ability to partially restore growth of *bm-8* on low-iron medium. The complementing region was narrowed by subcloning to a 1.1-kb Hind III fragment. M13 forward and reverse primers were used to sequence into the insert. The region was located on chromosome IV and shown to contain the entire open reading frame for YDL120w.
11. The complementing Hind III fragment was cloned into the centromeric vector M1188 YCP-URA pRS305, and the resulting construct was shown not to complement *bm-8* on low-iron medium. The Hind III fragment was also cloned into the yeast integrative plasmid YIP-LEU2 M1091. This construct was transformed into *bm-8*, and recombinants were selected on plates of complete minimal medium without leucine. The integration of *LEU2* next to *YFH1* was confirmed by Southern blot analysis. Recombinants were then mated to wild-type strain DY1457 and the diploids sporulated. Tetrad analysis revealed that the *LEU2* marker segregated independently of the *bm-8* phenotype of poor growth on low-iron medium.
12. *YFH1* was disrupted by insertion of a Bam HI fragment of the *HIS3* gene into the PflMI site of *YFH1*, creating plasmid MB1. A Sal I–Eco RI insert containing the disrupted *YFH1* reading frame was isolated and transformed into wild-type strain DY150. *YFH1* disruption candidates were selected on CM-his⁻ medium. Recombinants were verified by Southern blot analysis.
13. M. Babcock *et al.*, data not shown.
14. K. Nakai, *Bull. Inst. Chem. Res. Kyoto Univ.* **69**, 269 (1991).
15. A *YFH1* PCR product was generated with the added restriction sites Xba I and Cla I. The forward primer was 5′-GCTCTAGAGTGTAGCAATGATTAAGC-3′, and the reverse primer was 5′-CCATCGATTTG-GCTTTTAGAAATGGC-3′. The PCR product, digested with Xba I and Cla I, was cloned into the vector pGFP-C-FUS [R. K. Niedenthal *et al.*, *Yeast* **12**, 773 (1996)]. The resulting Yfh1p-GFP construct was transformed into *yfh1::HIS3*. The construct was able to complement the growth defect on YPD.
16. R. Stearman, D. S. Yuan, Y. Yamaguchi-Iwai, R. D. Klausner, A. Dancis, *Science* **271**, 1552 (1996).
17. Y. Yamaguchi-Iwai *et al.*, *EMBO J.* **14**, 1231 (1995).
18. L. Schols *et al.*, *Eur. J. Neurol.* **3**, 55 (1996).
19. E. Bonfoco *et al.*, *Proc. Natl. Acad. Sci. U.S.A.* **92**, 7162 (1995).
20. J. P. Blass *et al.*, *N. Engl. J. Med.* **295**, 62 (1976); U. J. Dijkstra *et al.*, *Ann. Neurol.* **13**, 325 (1983); D. A. Stumpf *et al.*, *Neurology* **32**, 221 (1982). Several abnormalities were reported and thought to be the primary defect in FRDA. These include lipoamide dehydrogenase deficiency, pyruvate carboxylase deficiency, and mitochondrial malic enzyme deficiency. Subsequent studies did not confirm that any of these abnormalities could be the primary defect in FRDA.
21. R. O. Morgan *et al.*, *Can. J. Neurol. Sci.* **6**, 227 (1979).
22. S. Chamberlain and P. D. Lewis, *J. Neurol. Neurosurg. Psychiatry* **45**, 1136 (1982).
23. J. B. Lamarche *et al.*, in *Handbook of Cerebellar Diseases*, R. Lechtenberg, Ed. (Dekker, New York, 1993), pp. 453–457. Stainable iron was identified in cardiomyocytes from all 15 FRDA patients that were examined and none from 10 controls. No iron deposits were present in the liver, in endocrine tissues, or in the reticuloendothelial system of FRDA patients.
24. G. Barbeau, *Can. J. Neurol. Sci.* **7**, 455 (1980).
25. A. E. Harding, *Adv. Neurol.* **61**, 1 (1993).
26. M. Ben Hamida *et al.*, *Neurology* **34**, 2179 (1993).
27. S. M. Thomas *et al.*, *Biochim. Biophys. Acta* **1002**, 189 (1989).
28. A. Filla *et al.*, *Am. J. Hum. Genet.* **59**, 554 (1996); A. Dürr *et al.*, *N. Eng. J. Med.* **335**, 1169 (1996); L. Montermini *et al.*, *Ann. Neurol.* **41**, 675 (1997).
29. C. C. Askwith and J. Kaplan, *J. Biol. Chem.* **272**, 401 (1997).
30. B. S. Glick and L. A. Pons, *Methods Enzymol.* **260**, 213 (1995).
31. Supported by grants from NIH (DK49219 and DK30534 to J.K., NS34192 to M.P.), by the Muscular Dystrophy Association (M.P.), and by the Fondation Notre Dame (M.P.). D.S. was supported by a NIH postdoctoral Hematology training grant (T32DK07115), and L.M. was supported by a Medical Research Council of Canada postdoctoral fellowship.

13 March 1997; accepted 6 May 1997

Bimolecular Exon Ligation by the Human Spliceosome

Karin Anderson and Melissa J. Moore*

Intron excision is an essential step in eukaryotic gene expression, but the molecular mechanisms by which the spliceosome accurately identifies splice sites in nuclear precursors to messenger RNAs (pre-mRNAs) are not well understood. A bimolecular assay for the second step of splicing has now revealed that exon ligation by the human spliceosome does not require covalent attachment of a 3′ splice site to the branch site. Furthermore, accurate definition of the 3′ splice site in this system is independent of either a covalently attached polypyrimidine tract or specific 3′ exon sequences. Rather, in this system 3′ splice site selection apparently occurs with a 5′ → 3′ directionality.

Introns in nuclear pre-mRNAs are removed by the spliceosome, a 60S complex composed of the pre-mRNA, four small nuclear RNAs (snRNAs) (U1, U2, U4-U6, and U5), and numerous associated proteins (*1*). Within this complex, intron excision occurs in two chemical steps, each comprising a single transesterification (*2*, *3*). First, the 2′-OH of the branch site adenosine attacks the 5′ splice site to release the 5′ exon and form a lariat intron intermediate. The newly freed 3′-OH of the 5′ exon then attacks the 3′ splice site to join the exons and displace the intron. However, the mechanism by which the spliceosome precisely targets these chemical reactions to bona fide splice sites in a milieu of potential cryptic sites is not clear.

Splice site recognition is especially problematic in mammals, in which genes are usually interrupted by multiple introns, often much longer than the exons, and splice site sequences are not highly conserved. The mammalian 5′ splice, branch, and 3′ splice (*4*) site consensus sequences are /GURAGU, YNYURAC, and $Y_{\geq 10}$NYAG/, respectively (where / denotes a splice site; N, any nucleotide; R, purine; Y, pyrimidine; and underlining, the most highly conserved positions) (*1*, *5*). The branch and 3′ splice sites are usually separated by 11 to 40 nucleotides (nt) because, in mammals, the polypyrimidine tract (PPT) portion of the 3′ splice site consensus is required for branch site definition (*6*).

Although the mechanisms that underlie recognition of the 5′ splice and branch sites have been studied extensively (*7*), much less is known about how the exact site of exon ligation is determined (*8*). In budding yeast, the 3′ splice site consensus is simply YAG/; there is no conserved PPT. However, even in these organisms, which have far shorter and far fewer introns than do mammals, trinucleotide recognition alone is clearly insufficient to ensure 3′ splice site fidelity, given that 1 of every 32 random trinucleotides is YAG. In most introns in yeast and all introns in mammals, the site of exon ligation is the first YAG downstream of the branch site (*9*), which suggests that branch site proximity is a key factor in 3′ splice site selection. Yet, in *Saccharomyces cerevisiae*, a second YAG downstream of the first can be the preferred exon ligation site if it is preceded by a region rich in pyrimidines (*10*). Thus, sequence context also contributes substantially to 3′ splice site use in yeast.

The relative contributions of branch site proximity and sequence context have been more difficult to evaluate in mammalian introns because the YAG most proximal to the branch site is generally preceded by a pyrimidine-rich region: the PPT. Because the PPT normally abuts the splice site YAG, it could be inferred that an adjacent

W. M. Keck Institute for Cellular Visualization, Department of Biochemistry, Brandeis University, Waltham, MA 02254, USA.

*To whom correspondence should be addressed. E-mail: mmoore@binah.cc.brandeis.edu